# SLHC-PP

# DELIVERABLE REPORT

## EU DELIVERABLE: 7.1.1

| | |
|---|---|
| Document identifier: | **SLHC-PP-7.1.1-982420-v1.0** |
| Contractual Date of Delivery to the EC | **End of Month 12 (March 2009)** |
| Actual Date of Delivery to the EC | **30/3/2008** |
| Document date: | **2/2/2008** |
| Deliverable Title: | **Finite element thermal study of the Linac 4 design source at the final duty factor** |
| Work package: | **WP7: Development of critical components for the injectors** |
| Lead Beneficiary: | **CERN** |
| Authors: | **M. Kronberger, J. Lettry, R.Scrivens** |
| Document status: | **Released** |
| Document link: | https://edms.cern.ch/document/982420/1 |

## History of Changes

| Version | Date | Comment | Authors |
|---------|------|---------|---------|
| 0.1 | 2009-02-09 | Creation of document | M. Kronberger |
| 0.1 | 2009-03-20 | First draft of document | M. Kronberger |
| 0.2 | 2009-03-23 | Second draft of document | M. Kronberger |
| 0.3 | 2009-03-25 | 3rd draft of document | M. Kronberger |
| 1.0 | 2009-03-30 | version 1.0 created | M. Kronberger |
|  |  |  |  |
|  |  |  |  |
|  |  |  |  |
|  |  |  |  |

## TABLE OF CONTENTS

## ABSTRACT

The temperature distribution and heat flow at equilibrium of the plasma generator of the non-cesiated Linac4 H⁻ ion source have been studied with a finite element model. It is shown that the equilibrium temperatures obtained in the Linac4 nominal operation mode (100 kW RF power, 2 Hz, 0.4 ms pulse duration) are within material specifications except from the magnet cage, where a redesign may be necessary. To assess the upgrade of the Linac4 source for operation in SPL, an extrapolation of the heat load towards the high-power option of the SPL nominal operation mode (100 kW RF power, 50 Hz, pulse duration 0.4 ms) has been performed. The results indicate the major improvements of the source cooling that are required to allow for operation in SPL.

## 1. INTRODUCTION

The Superconducting Proton Linac (SPL) is proposed to deliver beam to the future Proton Synchrotron (PS2), and will allow an increase in the beam brightness for LHC [1]. The LP-SPL (low-power SPL) uses an extension of the currently built Linac4 [2] as front-end, increasing the energy to a maximum of 5 GeV. The HP-SPL (high power SPL) option increases the duty cycle from about 0.1% to several percent, which would open physics possibilities for super-beams for neutrino production, muon production for a neutrino factory, or increased radioisotope production. This increase in repetition rate demands the development of a new RF H⁻ source. In particular, the new source needs to withstand the high thermal load experienced in the HP-SPL mode, which will be up to 75 times higher than in the nominal operation mode of Linac4 (Table 1).

*Table 1:* H⁻ source nominal operation modes at Linac4 and SPL. Typical values for the DESY -HERA RF source are shown for comparison.

|  | **Linac4** | **LP-SPL** | **HP-SPL** | **DESY** |
|---|---|---|---|---|
| H⁻ current [mA] | 80 | 80 | 80 | 40 |
| RF peak power [kW] | 100 | 100 | 100 | 30 |
| RF frequency [MHz] | 2 | 2 | 2 | 2 |
| repetition rate [Hz] | 2 | 2 | 50 | 3 |
| pulse length [ms] | 0.4 | 1.2 | 0.4 - 1.2 | 0.15 |
| duty factor [%] | 0.08 | 0.24 | 2 – 6 | 0.045 |
| Average RF power [W] | 80 | 240 | 2000 - 6000 | 13.5 |

This report presents the results of a thermal study of the plasma generator of the non-caesiated Linac4 H⁻ ion source [3], which is a slightly adapted version of the DESY-HERA RF source [4]. An outline of the Linac4 plasma generator is given in Fig. 1. Its main entities are: An ignition element used to ignite the plasma by means of an electrical arc; a plasma chamber made of $Al_2O_3$ ceramic; a copper antenna used to feed RF power into the plasma; a Delrin® magnet cage including an arrangement of 2 x 12 NdFeB cusp magnets and 10 NiZn ferrites; an extraction region comprising a magnetic filter and an adjustable collar; and a ceramic insulator that suspends the source body onto the vacuum tank.

Two operation modes of the plasma generator have been considered:

A)  Linac4 peak power operation mode (80W average RF power)

B)  Minimum HP-SPL operation mode (2kW average RF power)

Starting from these parameters, the equilibrium temperatures and heat fluxes determined by the simulations are used for identification of the critical parts of the system and, for the assessment of the cooling necessary to keep the individual source components within material specifications.
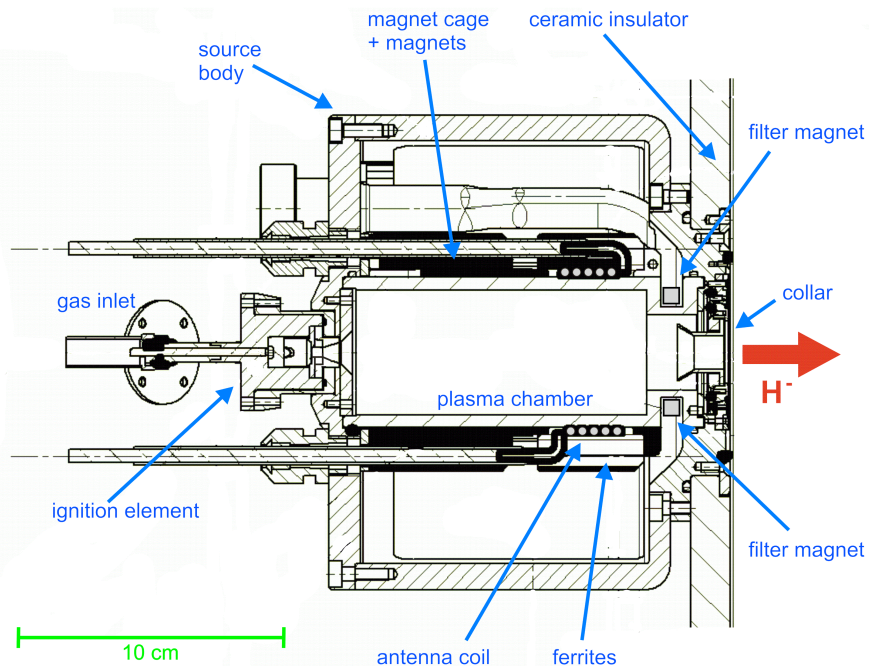


*Fig. 1: Outline of the Linac4 plasma generator.*

## 2.  THERMAL MODELING OF THE LINAC4 PLASMA GENERATOR

The temperature distribution and the heat flux at equilibrium in the plasma generator have been studied by finite element modelling (FEM) using the ANSYS and ANSYS Workbench software packages. Two counteracting processes have been considered:

(1) Heating of the inner surfaces of the plasma generator by absorption of thermal radiation from the plasma and, by electrical power from plasma ignition;

(2) Cooling of the outer surfaces of the plasma generator by convection and by the emission of thermal radiation.

All the RF power is assumed to be delivered to the plasma. Furthermore, the time dependence of the heat load (which is due to the pulsed mode operation of the plasma source) has not been modelled and only an average heat load has been considered. Other phenomena that have not been accounted for in the simulations include thermal expansion,

thermally induced stresses, plasticity, and phase changes (boiling, melting) of the materials, and the sub-millisecond plasma rise time.

## 2.1. HEAT SOURCES

The heat flux from the plasma towards the inner surfaces of the plasma generator is a function of the plasma temperature and density and their spatial distribution. An additional small contribution to the total heat flux that is relevant in particular for the ignition element is the electrical power needed for plasma ignition. In the following, the treatment of both processes in the simulations is shortly discussed.

### 2.1.1.    Thermal load from hydrogen plasma

The thermal load originating from the hydrogen plasma depends on the coupling of the RF power delivered to the plasma. However, it is not straightforward to determine which fraction of RF power is absorbed by the plasma or by the metallic components of the plasma generator, or simply radiated away. For this reason, the simulations were primarily based on a conservative scenario in which the entire RF power (table 1) is transmitted to the plasma volume. As a first approximation, it was postulated that the thermal radiation emitted by the plasma originates from an ellipsoidally shaped region centred at the RF antenna coil, i.e. in the region where the transfer of RF power to the plasma is believed to reach a maximum. The temperature of the ellipsoid, $T_{ell}$, was set to a value for which the relation

$$\sigma \cdot (T_{ell}^4 - T_{env}^4) = \frac{q_{RF}}{A_{ell}} \qquad \text{(I)}$$

was fulfilled, where $q_{RF}$ is the average RF power transmitted to the plasma, $A_{ell}$ the surface area of the ellipsoid, $\sigma$ the Stefan-Boltzmann-constant, and $T_{env}$ the environmental temperature. The power delivered to the element $i$ by thermal radiation from the plasma was then determined by the relations

$$q_i = q_{RF} \cdot F_{e,i} \qquad \text{(II)}$$

and

$$\sum_i F_{e,i} = 1 \qquad \text{(III)}$$

Where $q_i$ is the power incident on the surface of element $i$ and $F_{e,i}$ the view factor between this surface and the surface of the plasma ellipsoid. The surfaces heated by the plasma are schematically shown in Fig. 2; the calculated thermal loads are summarized in table 2. The heat load distribution on the inner wall of the ceramic plasma chamber is indicated in Fig. 3.
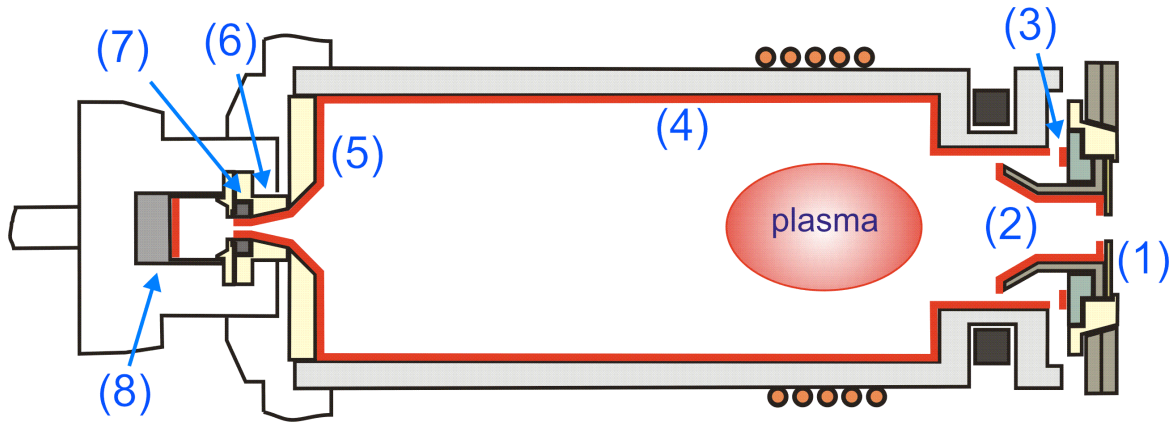
*Fig. 2: Parts and surfaces exposed to radiation from the plasma. (1) plasma aperture electrode; (2) funnel electrode; (3) closing disk; (4) plasma chamber cylinder; (5) plasma chamber rear plate; (6) clamp collar; (7) anode; (8) cathode. Parts (1) - (3) are part of the collar, parts (6) – (8) belong to the ignition element. The plasma ellipsoid used for the calculations is indicated in the sketch; irradiated surfaces are shown in red.*

*Table 2: thermal loads $q_i$ from hydrogen plasma. The numbers of the parts correspond to those in Fig. 2.*

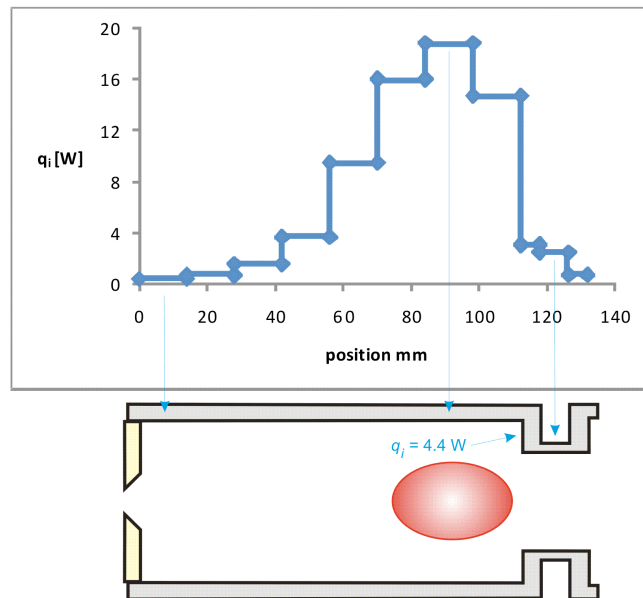| assembly | part | name | $F_{e,i} = q_i/q_{RF}$ | $q_i$ [W] | |
|---|---|---|---|---|---|
| | | | | Linac4 ($q_{RF}$ = 80W) | HP-SPL ($q_{RF}$ = 2kW) |
| collar | 1 | plasma aperture electrode | $1.8 \cdot 10^{-3}$ | 0.14 | 7 |
| | 2 | funnel electrode | 0.019 | 1.5 | 75 |
| | 3 | closing disks | 0.016 | 1.3 | 63 |
| plasma chamber | 4 | cylinder | 0.9525 | 76 | 3810 |
| | 5 | rear plate | $9.2 \cdot 10^{-3}$ | 0.74 | 37 |
| ignition element | 6 | clamp collar | $3.2 \cdot 10^{-4}$ | 0.026 | 1.3 |
| | 7 | anode | $1.8 \cdot 10^{-5}$ | $1.5 \cdot 10^{-3}$ | 0.07 |
| | 8 | cathode | $7.6 \cdot 10^{-5}$ | $6 \cdot 10^{-3}$ | 0.305 |

*Fig. 3: Simulated heat load distribution along the axial surfaces of the plasma chamber cylinder. The heat load of the only radially oriented surface that is heated up by the plasma ($q_i$ = 4.4 W) is indicated in the plot.*

### 2.1.2.    Thermal load from plasma ignition

The electrical energy necessary for plasma ignition was estimated from the nominal electrical parameters of the DESY H⁻ source ($U_0$ = 800V, C = 1μF) to be 0.6 J/pulse, which corresponds to a time average thermal load of 1.2 W for the 2 Hz repetition rate in Linac4 (table 3). This power was applied to the cathode and anode of the ignition element to account for the additional heat flow originating from plasma ignition. The heat flow was distributed between cathode (60%) and anode (40%) to account for the different energy transfer mechanisms of ions and electrons.

It shall be noted that the design of the ignition element used in the DESY H⁻ source was changed recently, leading to a reduction of the electrical power by a factor of 30. Although this new design has not been included yet in the Linac4 plasma generator, a similar system will be used in the future. For this reason, this reduced thermal load has been used in the simulations with the HP-SPL thermal load.

*Table 3: nominal electrical parameters of the ignition element in the DESY H⁻ source. The electrical energy per pulse has been reduced for HP-SPL to account for an improved model, as noted in the text.*

|  | Linac4 | HP-SPL |
|---|---|---|
| energy/pulse [J] | 0.6 | 0.02 |
| pulse length [μs] | 40 | 40 |
| repetition rate [Hz] | 2 | 50 |
| duty factor (%) | 0.008% | 0.2 - 0.6% |
| average power [W] | 1.2 W | 2.5 - 7.5 W |

## 2.2. COOLING MECHANISMS

Various cooling mechanisms have been taken into account for the outer surfaces of the plasma generator.

*Surfaces exposed to vacuum* have been assumed to be cooled purely by the emission of thermal radiation. The power $q_S$ radiated away from a surface with area $A_S$ and temperature $T_S$ is given by

$$q_S = \varepsilon \cdot \sigma \cdot (T_S^4 - T_{env}^4) \cdot A_S \qquad \text{(IV)}$$

where $\varepsilon$ the hemispherical total emissivity of the material. As $\varepsilon$ not only depends on the material but also on the surface state, an average value has been used in cases where the exact surface state was not known. However, the importance of thermal radiation for the cooling is only small at temperatures of less than 500 K and $\varepsilon$ has only little effect on the outcome. Table 4 lists the emissivities and other properties of the materials of the source which were used in the simulations.

For *surfaces exposed to plain air,* convection has been taken into account as an additional cooling mechanism. The temperature dependence of the heat transfer coefficient of convective cooling, $HTC_{convection}$, has been modeled in first approximation by using a power law of the form [5]

$$HTC_{convection} \propto (T_S - T_{env})^{1/4} \qquad \text{(V)}$$

For bodies in contact with an *external heat sink* (e.g. the source housing), an $HTC_{convection}$ of typically 100000 W/m²K was assumed for the connecting surface. This value corresponds approximately to the HTC observed at the interface between two materials that are tightly screwed together.

*Table 4: Selected thermal and mechanical properties of materials used in the Linac4 plasma generator.*

| material | k [W/mK] | ε | $H_V$ [GPa] | refs | used in |
|---|---|---|---|---|---|
| SS-316L | 13.87 (300K) | 0.4 | 1.4 | [9,10,11] | source body |
| | 18.32 (600K) | | | | collar |
| | 32.36 (1600K) | | | | Ignition element |
| Copper | 402 (300K) | 0.2 | 0.5 | [9,10] | antenna, wires |
| | 374 (700K) | | | | |
| | 342 (1200K) | | | | |
| Titanium | 20.5 (280K) | 0.3 | 0.6 | [9,10] | cathode |
| | 18.6 (500K) | | | | collar |
| | 18.8 (1000K) | | | | |
| Molybdenum | 141 (300K) | 0.13 | 2.3 | [9,10,11] | anode |
| | 124 (500K) | | | | |
| | 100 (1400K) | | | | |
| NiZn ferrite [1] | 3.5 - 5 | 0.8 | 0.8 - 0.9 | [7,11] | ferrites |
| NdFeB [2] | 15 - 50 | 0.1 [4] | 3.5 [4] | [8,11] | filter magnets |

| | | | | | cusp magnets |
|---|---|---|---|---|---|
| Mica | 0.5 (293K) | 0.75 | 0.7 [5] | [9,10,11] | collar |
| | 2.1 (523K) | | | | |
| | 2.5 (900K) | | | | |
| fused silica | 1.4 (293K) | 0.8 | 6 | [9,15] | ignition element |
| | 1.6 (473K) | | | | |
| | 2.7 (1223K) | | | | |
| $Al_2O_3$ Ceramic [3] | 34.9 (293K) | 0.9 | 23 | [11,12] | plasma chamber |
| | 6.8 (1273K) | | | | front plate |
| | 5.3 (1773K) | | | | screws |
| Macor® | 1.45 (300K) | 0.8 | 2.5 | [11,13] | ignition element |
| | 1.35 (600K) | | | | collar electrode |
| | 1.5 (850K) | | | | |
| DuPont Delrin® | 0.36 | 0.3 | 0.18 [5] | [10,17] | magnet cage |
| Polyethylene | 0.33-0.52 | 0.3 - 1 | 0.05 [6] | [14,16,17] | antenna shrink tubes |
| DuPont Viton® | 0.2 | - | 0.05 [6] | [10] | o-rings |

Notes: [1] 8C11 (FerroXCube); [2] Vacodym 633HR (Vacuumschmelze), Ni coated; [3] Frialit (Friatec); [4] values of Ni coating used; [5] derived from shear strength; [6] derived from tensile strength.


## 2.3. HEAT TRANSPORT IN THE PLASMA GENERATOR

Three processes of heat transport have been considered in the simulations:

(1) Thermal conduction inside a material

(2) Heat transfer through physical contacts

(3) Heat transfer by thermal radiation


### 2.3.1.      Thermal conduction

Thermal conduction inside the plasma generator was modelled by the thermal conductivities $k$ of the materials. Typically, $k$ is a function of temperature and may also depend on the orientation of the crystal lattice. In the simulations, $k$ has been assumed to be isotropic. The temperature dependence of $k$ has been modelled in cases where data on $k$ for more than one temperature were available; otherwise, a constant value of $k$ has been used.

### 2.3.2.      Contacts

An important problem in heat flow simulations is the correct modelling of the heat transfer between two entities that are in close contact with each other. In particular, it becomes challenging when important parameters, for example the contact pressure or the width of a gap between two surfaces, are only approximately known. Moreover, the contact heat transfer coefficient $HTC_{contact}$ is usually a function of temperature due to thermal expansion and the increase in thermally radiated power at higher temperatures.

As the complexity of the model (and therefore, the calculation time) would increase rapidly with these processes considered (there are more than 200 individual contacts in the model),

$HTC_{contact}$ was assumed to be constant for each contact. This assumption holds especially for low temperatures (< 200°C) and $\Delta T \leq 100$°C as the change in $HTC_{contact}$ is expected to be small compared to its value in this range.

Because of the lack of experimental data for benchmarking, approximate contact heat transfer coefficients were determined from theoretical models. In cases where the surfaces of two elements were in physical contact, $HTC_{contact}$ was estimated by the law of Cooper et al. [6],

$$HTC_{contact} = 1.45 \cdot \frac{m \cdot k}{\sigma_s} \left( \frac{P}{H_V} \right)^{0.98} \qquad (VI)$$

where $P$ is the contact pressure, $H_V$ the mean Vickers microhardness, $m$ the mean surface asperity slope, and $\sigma_s$ the mean RMS surface roughness of the materials.

In cases where two components where not in physical contact, but separated by a thin (<1 mm) air-filled gap, $HTC_{contact}$ was determined from a gap conductance model [5], which reduces in first approximation to

$$HTC_{contact} \approx \frac{1}{2\sqrt{2}} \frac{k_a}{d} \qquad (VII)$$

when the gap width $d \gg \sigma, m$. $k_a$ = 0.024 W/m·K is the thermal conductivity of air.

### 2.3.3.    Thermal radiation

The exchange of heat by thermal radiation has been taken into account for surfaces separated by more than 1mm in air and for surfaces in an evacuated area that are not in physical contact. The net heat exchange between two bodies with temperatures $T_1$ and $T_2$ is given by [5]

$$q_1 = A_1 \cdot \Im_{1,2} \cdot \sigma \cdot (T_1^4 - T_2^4) \qquad (VIII)$$

where $A_1$ is the surface area of body 1 and $\Im_{1,2}$ a generalized view factor that takes also the emissivities of the two bodies into account.

## 3.  RESULTS

The main parameters determined by the thermal simulations are (1) the equilibrium temperature, and (2) the heat flux inside the Linac4 plasma generator. While the temperature distribution can be used to validate general material specifications and to estimate thermal expansion and thermal stresses, the heat flux indicates where the heat transport is efficient and where it is not. Both parameters can be used to assess which improvements of geometry or design are necessary to optimize heat transport.

### 3.1. LINAC4 SETTINGS (100KW, 0.08% DUTY CYCLE)

#### 3.1.1.    Temperatures

The overall temperature distribution inside the plasma generator operated under nominal Linac4 conditions is depicted in Fig. 4. Equilibrium temperatures obtained for different components of the H$^-$ source range from room temperature to a maximum of 135$^o$C. The highest temperatures are found in the vicinity of the antenna coil.

In the following, the main parts of the source are discussed individually.

**Plasma chamber (Fig. 5):** The $Al_2O_3$ plasma chamber exhibits a moderate temperature gradient from 135$^o$C near the antenna position to 75 – 80$^o$C at both ends.

**Collar electrode (Fig. 6):** The highest temperature (95$^o$C) is found at the tip of the funnel electrode. Neither thermal stresses nor problems due to thermal expansion are expected.

**Antenna (Fig. 7):** Temperatures in the antenna range from 125$^o$C at the central winding of the antenna coil to 30$^o$C at the tips. The temperatures observed for the antenna rods are generally <70$^o$C which is within the allowed working range of the plastic shrink tubes that are used for insulating the rods [14]. However, it shall be noted that power dissipation in the antenna has not been included in the simulations and the actual temperatures experienced during Linac4 operation are probably higher.

**Ignition element (Fig. 8):** Temperatures are generally non-critical and range from 50$^o$C to 75$^o$C.

**Magnet cage (Fig. 9):** Temperatures of up to 125$^o$C are observed at the inner surfaces in the vicinity of the antenna. As this is well above the maximum allowed temperature for this material (100$^o$C) a redesign of the magnet cage, the use of a material with better thermal conductivity or better resistance to heat, or an improvement of the cooling is necessary to run at this power level.

**Ferrites and magnets (Fig. 10):** Temperatures observed in the ferrites and the magnets are below their maximum allowed working temperature (Ferrites: 125$^o$C; magnets: 110$^o$C [7,8]). However, the actual temperatures during Linac4 operation may be higher due to currents induced by the RF and demagnetisation may take place.
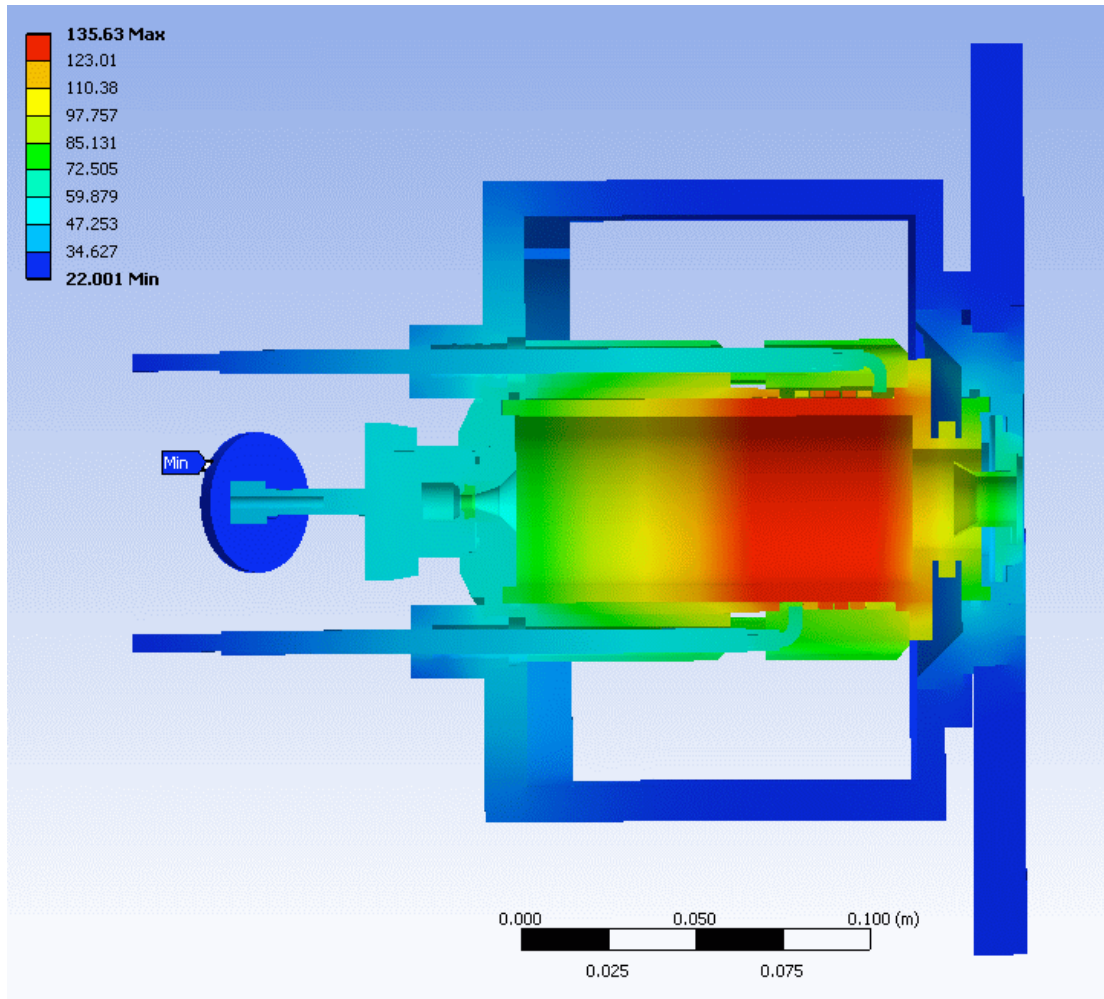
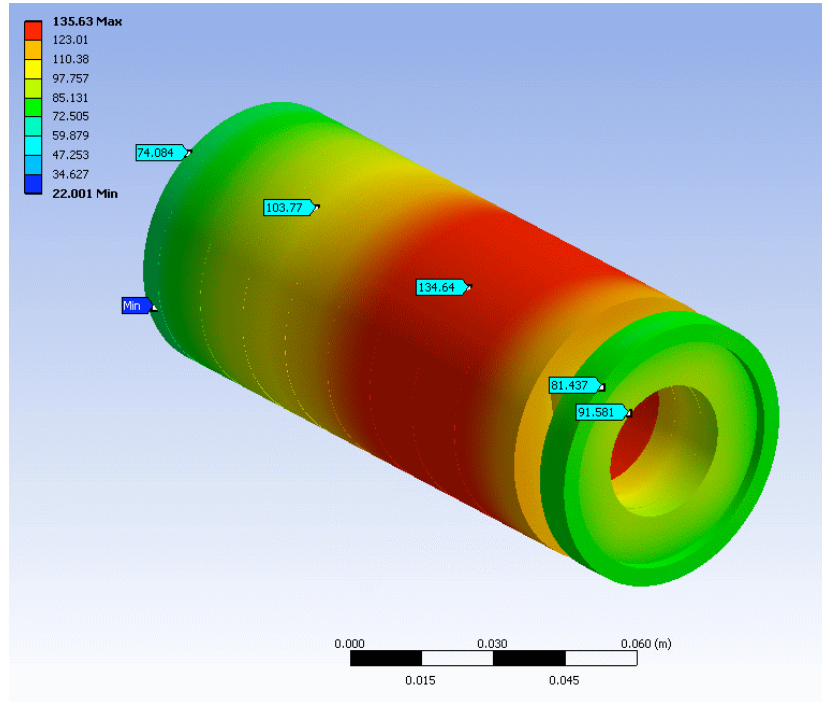*Fig. 4: Temperature distribution in the Linac4 plasma generator, $q_{RF}$ = 80W.*

*Fig. 5: Temperature distribution: $Al_2O_3$ plasma chamber, $q_{RF}$ = 80W.*
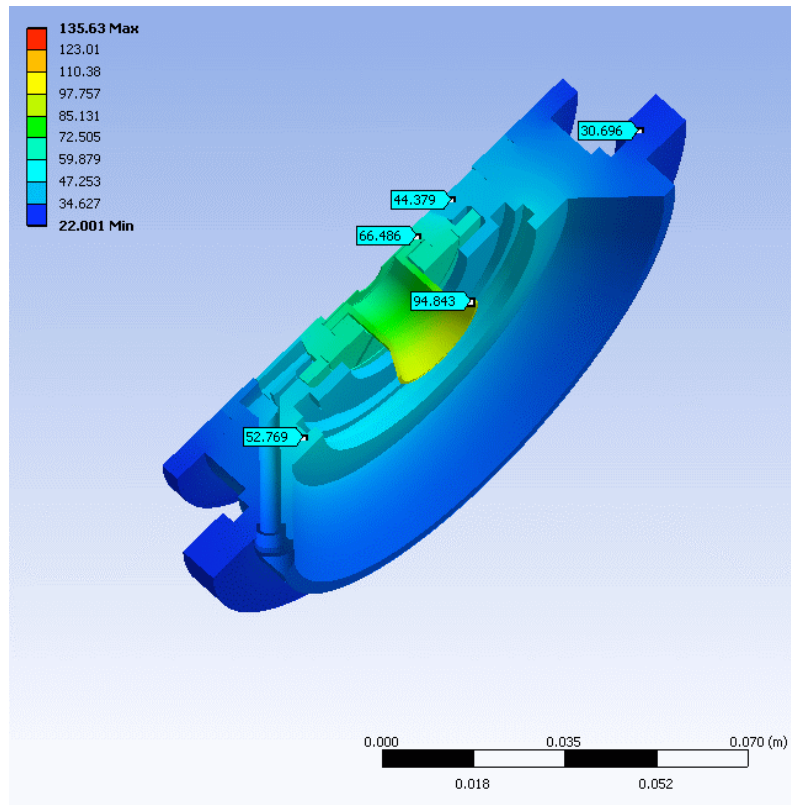


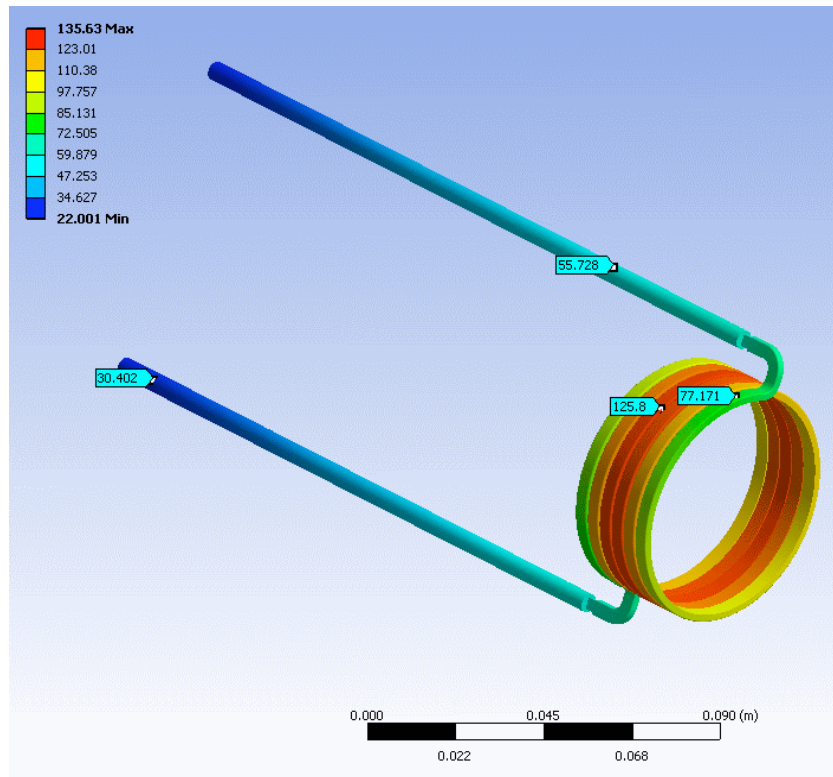*Fig. 6: Temperature distribution: collar electrode, $q_{RF}$ = 80W.*

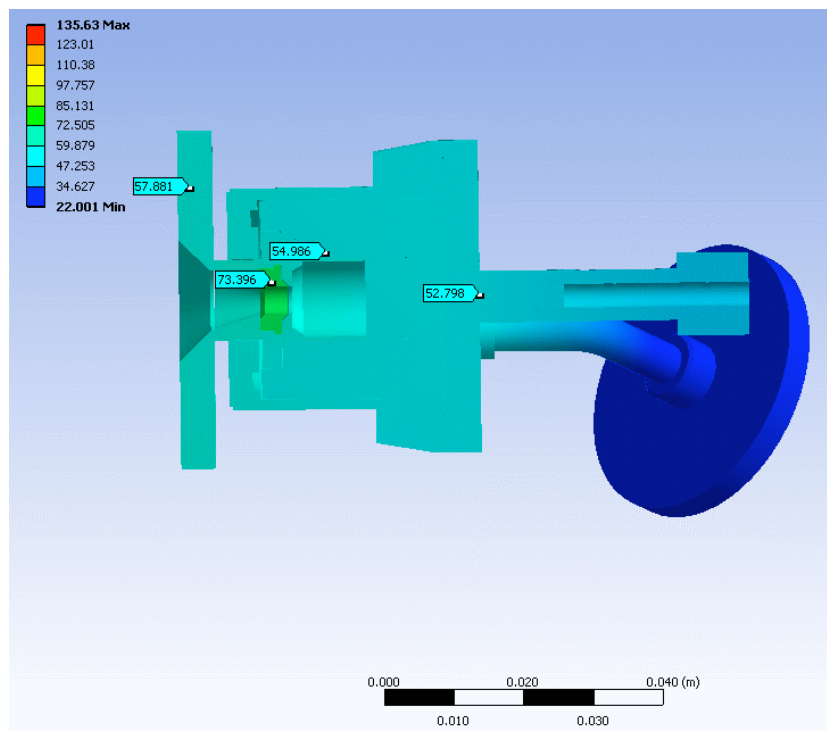Fig. 7: Temperature distribution: antenna, $q_{RF}$ = 80W.



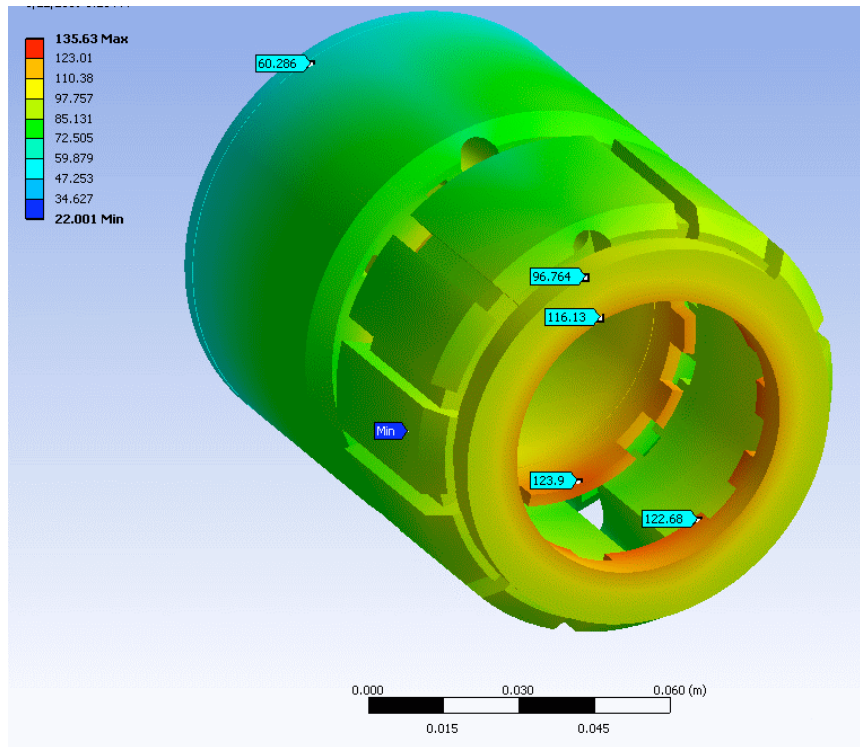Fig. 8: Temperature distribution: ignition element, $q_{RF}$ = 80W, $q_{ignition}$ = 1.2 W.

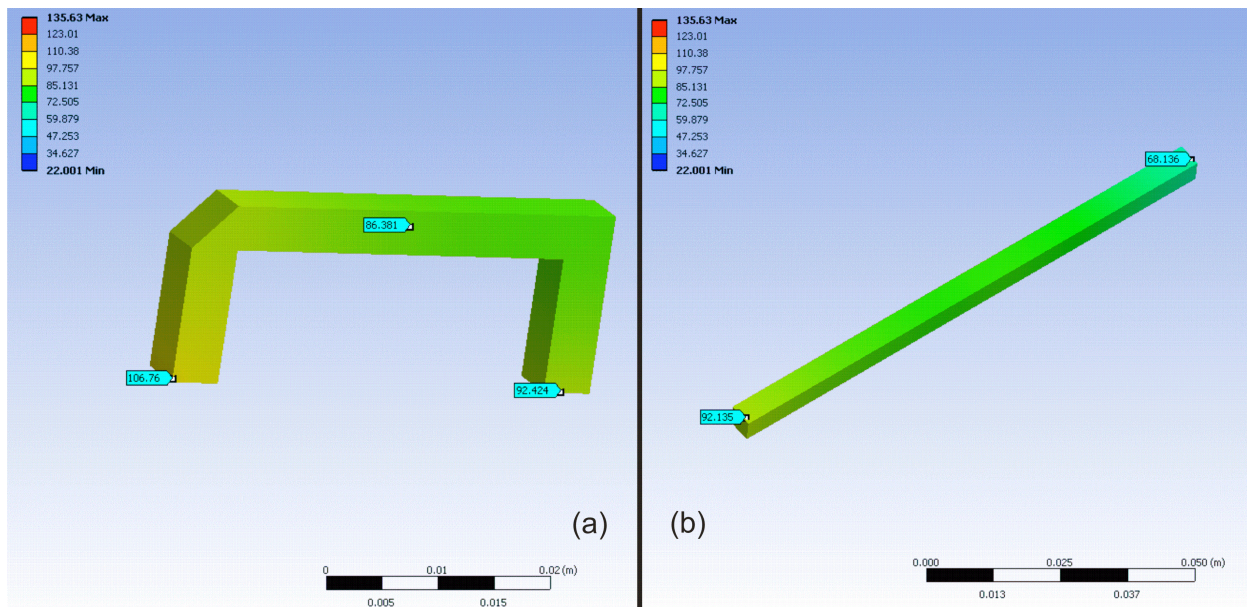*Fig. 9: Temperature distribution: Delrin magnet cage, $q_{RF}$ = 80W.*



*Fig. 10: Temperature distribution: (a) Ferrites, (b) magnets, $q_{RF}$ = 80W.*

### 3.1.2.    Heat flux

The total, axial, and radial heat fluxes observed in the Linac4 plasma generator at 80W are shown in Figs. 11 and 12.

Most of the heat produced by the plasma flows in the axial direction towards the collar and the ignition source of the plasma generator, which underlines the need of using materials with high thermal conductivity for the plasma chamber and the components that are in direct contact with it. As soon as the ends of the plasma chamber are reached, the direction of the heat flow changes from axial to radial. Heat that has been transported towards the collar then moves towards the $Al_2O_3$ front plate and the heat sink connected to its end, while heat that has been transported towards the ignition source moves into the steel housing of the plasma generator from where it is removed by convective heat exchange with the surrounding air and the emission of thermal radiation. On the other hand, the radial outflow of heat from the plasma chamber is suppressed by the low thermal conductivity of the Delrin magnet cage, which acts effectively as a thermal insulator. This implies that the temperature of the plasma chamber could be lowered further by using a material with higher thermal conductivity for the magnet cage.
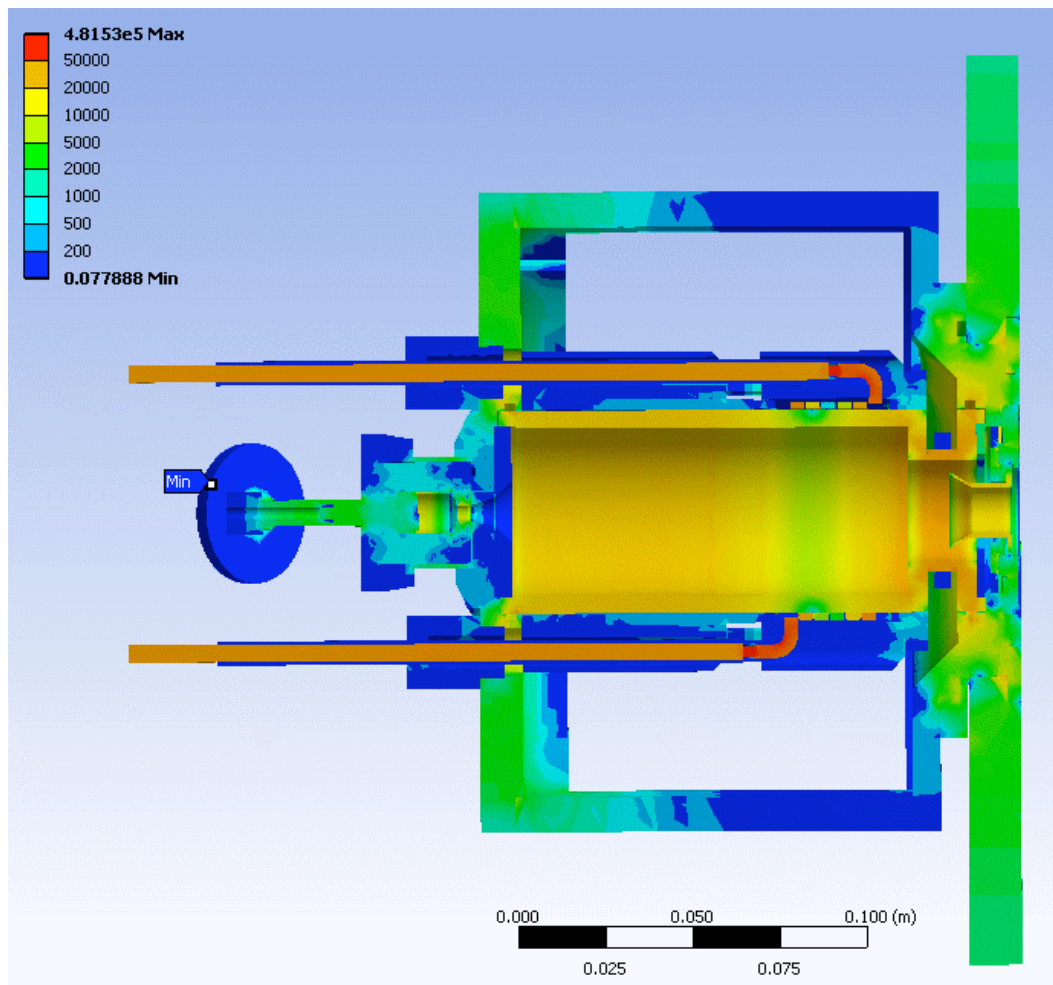


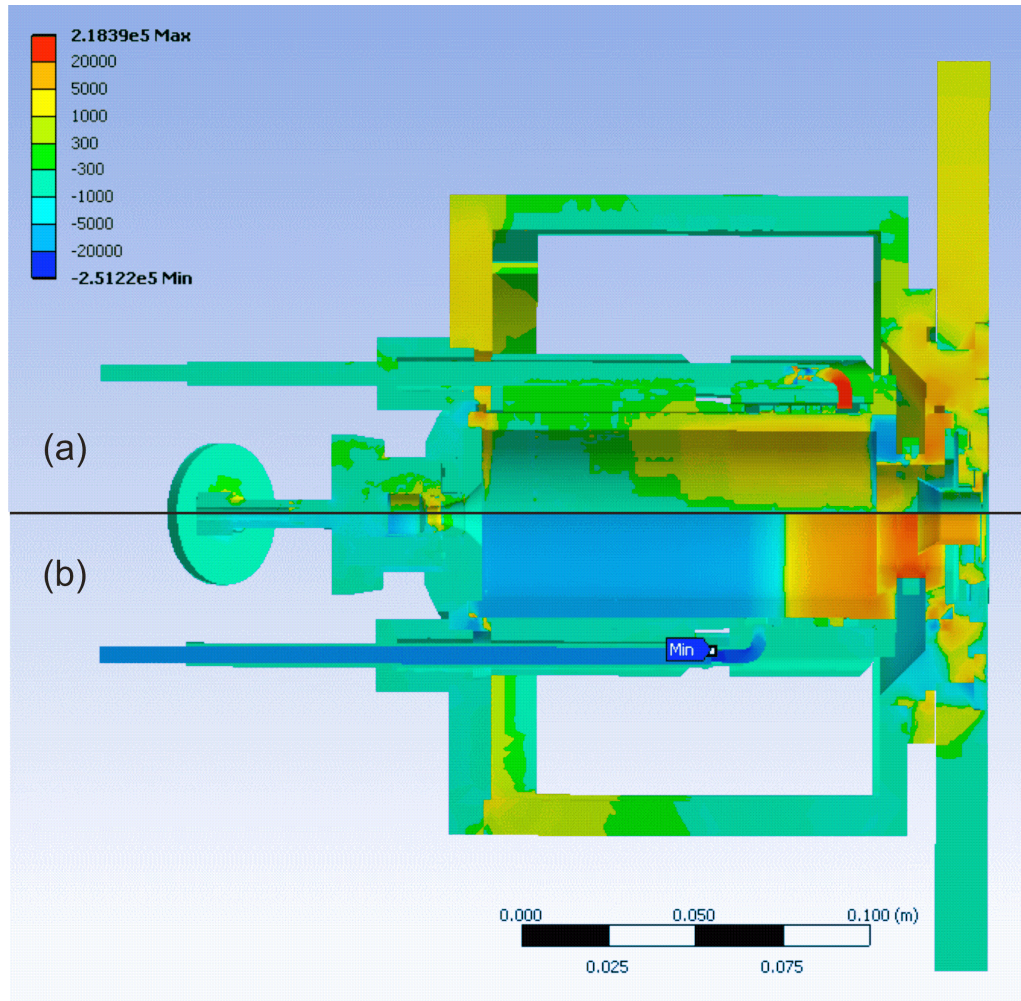*Fig. 11: total heat flux, $q_{RF}$ = 80 W.*

*Fig. 12: Heat flux in (a) radial and (b) axial direction, $q_{RF}$ = 80 W.*

## 3.2. HP-SPL SETTINGS (100 KW, 2% DUTY CYCLE)

The priorities and critical regions for the thermal engineering of the SPL plasma generator will be based on the analysis of the heat flow pattern and temperature distribution. As a first step, the simulation of the Linac4 plasma generator submitted to the lower limit of the HP-SPL nominal heat load is presented below.

### 3.2.1.     Temperatures

The temperature distribution in the plasma generator under nominal HP-SPL operation conditions is presented in Figs. 13 to 15.

Obviously, the Linac4 plasma generator is not suited for the HP-SPL average power. Temperatures above 4000 K are reached in the plasma chamber (Fig. 14), the collar electrode (Fig. 15a), and the ignition element (Fig. 15b). Although the results are surely over-quantified due to the simplified model, it becomes obvious that the plasma generator would not survive the harsh operating conditions at HP-SPL.
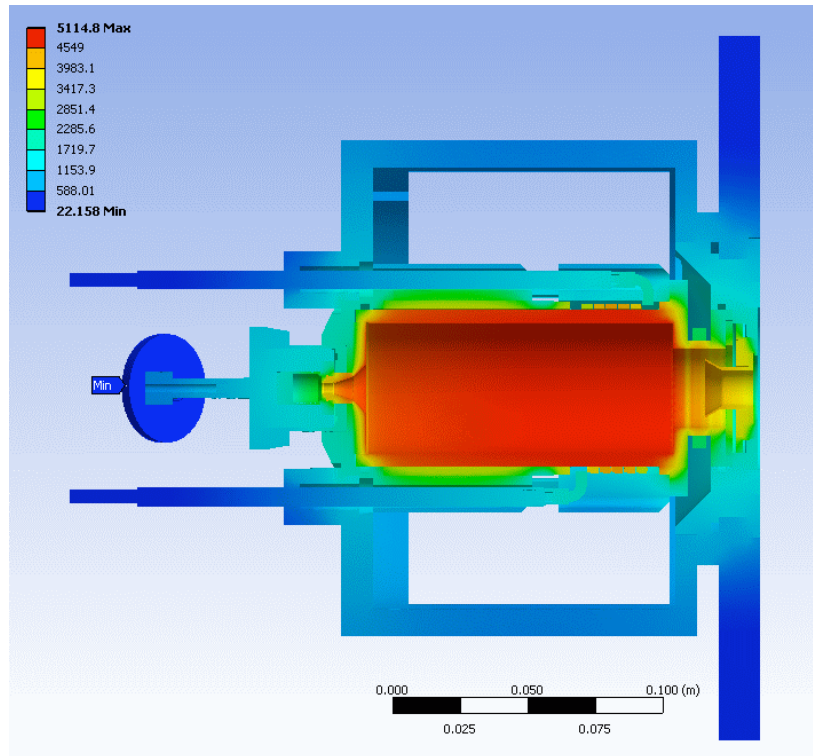
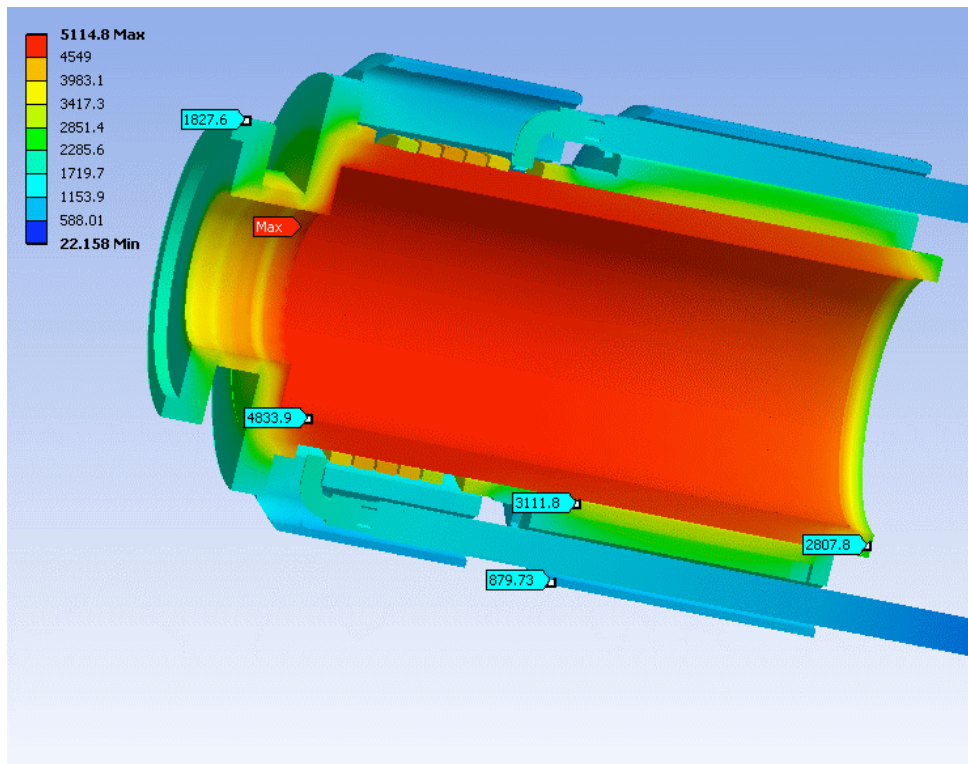*Fig. 13: Temperature distribution in the Linac4 plasma generator, $q_{RF}$ = 2 kW.*



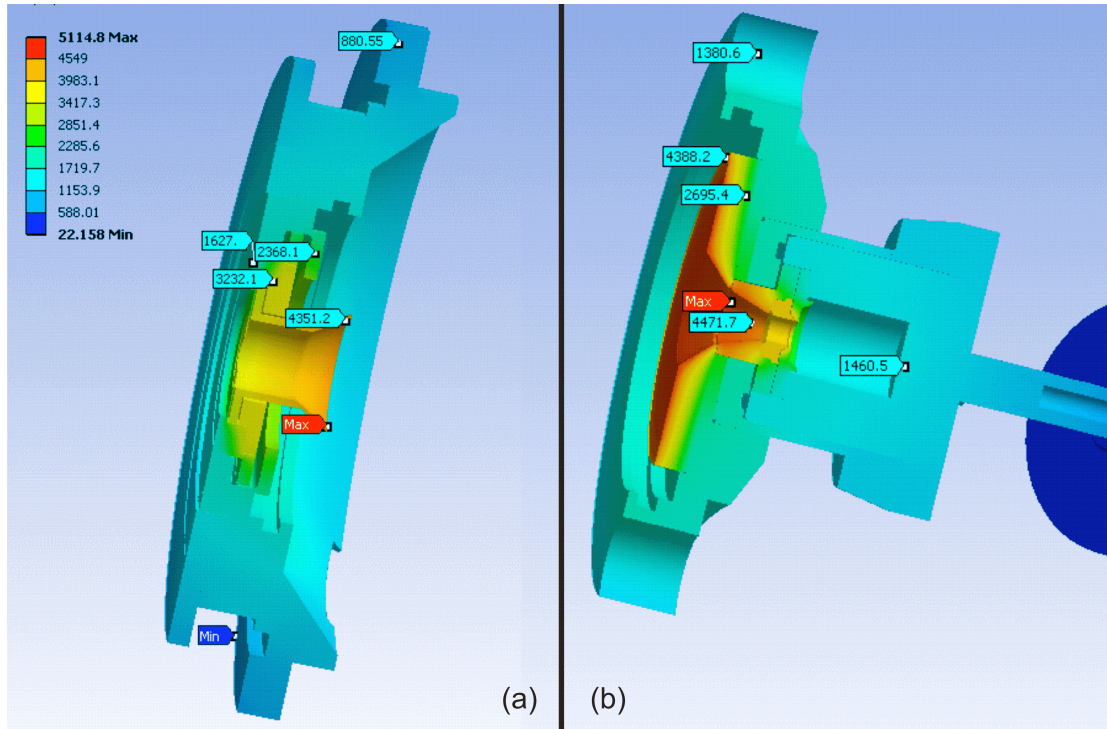*Fig. 14: Temperature distribution: plasma chamber and magnet cage, $q_{RF}$ = 2 kW.*

*Fig. 15: Temperature distribution: collar electrode (a) and ignition element (b). $q_{RF}$ = 2 kW, $q_{ignition}$ = 2.5 W.*

### 3.2.2. Heat flux

The reason for the immense over-heating of the Linac4 plasma generator under nominal HP-SPL operation condition becomes clear when the heat flux inside the plasma generator is assessed (Figs. 16 and 17). By comparing the radial and axial heat fluxes with those observed for the Linac4 operation mode, it becomes obvious that the radial outflow of heat from the plasma chamber is stronger in the SPL operation mode relative to the axial flow. In other words, the axial outflow of heat is less efficient than in the Linac4 operation mode. By a major part, this is a consequence of the small cross-section of the chamber wall, the strong decrease of the thermal conductivity of $Al_2O_3$ with temperature (Table 4), and limitations of the thermal contacts between the plasma chamber and the thermal masses of the source body and the $Al_2O_3$ front plate. Because of this, the heat is transported away mainly in radial direction, which, as discussed before, is a very inefficient process due to the thermally insulating properties of the Delrin magnet cage. This implies that a source of the same type requires a plasma chamber which (a) is made of a material with higher thermal conductivity than $Al_2O_3$ (for example AlN) to optimize heat transport, and (b) has active cooling on the outside surfaces implemented. Furthermore, the high temperature gradients observed in some of the components of the ignition element and the collar electrode imply that high thermal conductivity materials should preferably be used throughout the source.
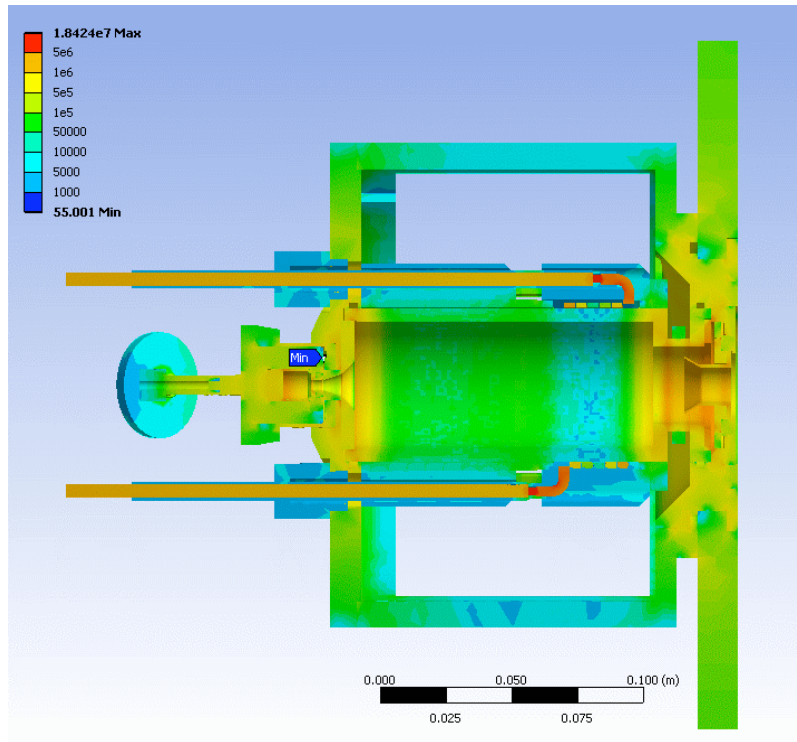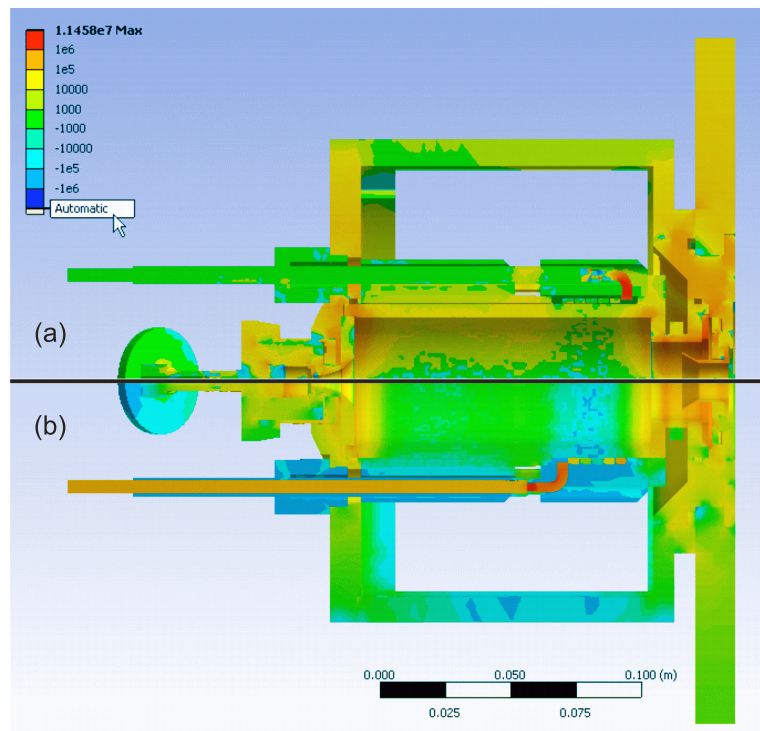
*Fig. 16: total heat flux, $q_{RF}$ = 2 kW.*



*Fig. 17: Heat flux: (a) radial direction, (b) axial direction, $q_{RF}$ = 2 kW.*

## 4. CONCLUSIONS

A FEM thermal study has been performed for the Linac4 H⁻ plasma generator for the nominal operation modes of Linac4 (100kW RF power, 0.08% duty cycle) and HP-SPL (100kW RF power, 2% duty cycle). Neither the thermal properties of the plasma, the time structure of the applied power, nor inductive heating of the metallic components have been taken into account and may influence the outcome. Within our assumptions, it is shown that:

***Linac4 ion source***: In its peak power operation mode, the equilibrium temperature of the Delrin magnet cage is critical and should be monitored. Eventually, a redesign of the magnet cage, an improvement of the cooling, or the use of different materials with better thermal conductivity are required if 100 kW RF power is necessary to reach the nominal Linac4 H⁻ current of 80 mA. The temperature of the magnets and the ferrites is below $T_C$ in the simulations but may rise up to this value due to inductive heating.

***Heat flow:*** Most of the heat produced by the plasma is removed in axial direction and only a small fraction in radial direction due to the low thermal conductivity of the Delrin magnet cage. Therefore, using materials with higher thermal conductivity for the ceramic plasma chamber cylinder, electrical insulators and the magnet cage is essential to improve the heat flow in the plasma chamber and reduce the peak temperatures.

***SPL plasma chamber:*** For an average heat flow of 2kW, which is the lower limit of the HP-SPL operation mode, the observed equilibrium temperatures are too high and an operation of the Linac4 plasma generator in the HP-SPL is excluded. The development of a high duty factor RF H⁻ ion source relies on a major engineering optimization of the thermal conductivity and geometry for each component of the plasma chamber and the engineering of water cooling that can be inspired of the one developed for the caesiated SNS H⁻ source.

***Outlook:*** Specific interface heat transfer coefficients needs to be measured to benchmark the simulation software and to identify suitable pressure and surface roughness. The Linac4 plasma chamber temperature could be monitored to allow a direct comparison to the simulation. An active water-cooling will be designed for the SPL plasma chamber and the thermal conductivities of the materials used in the source will be optimized (i.e. replacement of $Al_2O_3$ by AlN). Furthermore, the results obtained with plasma (i.e. Vorpal or TrapCad), RF-coupling (i.e. HFSS) and magnetic field (i.e. OPERA) simulation codes should contribute to the refinement of our heat source distribution hypothesis. With these actions being taken, we are confident to develop an RF powered H⁻ source that reproduces the excellent performance parameters of the Linac4 source and withstands the high thermal load in HP-SPL at the same time.

## REFERENCES

[1] M. Baylac et al., Conceptual Design of the SPL II: A high-power superconducting H⁻ linac at CERN. CERN-2006-006

[2] L. Arnaudon et al., Linac4 Technical Design report. CERN-AB-2006-084 ABP/RF

[3] D. Küchler, T. Meinschad, J. Peters, R. Scrivens, A radio frequency driven H⁻ source for Linac4. Rev. Sci. Instr. 79, 02A504 (2008)

[4] J. Peters, The HERA volume H⁻ source. PAC05 conference proceedings, 788 (2005)

[5]  W. M. Rohsenow, J. P. Hartnett, Y. I. Cho (eds.), Handbook of Heat Transfer, Third Edition. McGraw-Hill (1998)

[6]  M. G. Cooper, B. B. Mikic, M. M. Yovanovich, Thermal Contact Conductance. Int. J. Heat Mass Transfer 12, 279 (1969)

[7]  Ferrite type 8C11 Data sheet, FerroXCube, USA

[8]  Vacodym 633 HR Data sheet, Vacuumschmelze GmbH & Co. KG, Germany

[9]  Y. S. Touloukian (ed.), Thermophysical properties of matter. Plenum, New York, USA (1995)

[10] MatWeb material data base, http://www.matweb.com

[11] Transactions in measurement and control, Omega Engineering Inc., USA (http://www.omega.com/literature/transactions)

[12] Frialit data sheet, Friatec AG, Germany

[13] Macor data sheet, Corning Inc, New York, USA

[14] SZH data sheet, Srati, France

[15] Data sheet, glass dynamics, LLC, NJ, USA

[16] Data sheet, San Diego Plastics, Inc., CA, USA

[17] Autodesk® Ecotect™ WIKI, http://squ1.org/